Electronic Supplementary Material (ESI) for Nanoscale.

Supplementary Information for

Phonon transport in nano-system of Si and SiGe films with Ge nanodots and approach to ultralow thermal conductivity

Tatsuhiko Taniguchi,[1] Tsukasa Terada,[1] Yuki Komatsubara,[1] Takafumi Ishibe,[1] Kento Konoike,[1] Atsushi Sanada,[1] Nobuyasu Naruse,[2] Yutaka Mera,[2] and Yoshiaki Nakamura[1]*

[1] Graduate School of Engineering Science, Osaka University, 1-3 Machikaneyama-cho, Toyonaka, Osaka 560-8531, Japan

[2] Department of Fundamental Bioscience, Shiga University of Medical Science, Otsu, Shiga 520-2192, Japan

E-mail: nakamura@ee.es.osaka-u.ac.jp

Section S1: The spatial distribution of nanodots.

To investigate the spatial distribution of nanodots (NDs) in the films, scanning tunneling microscopy (STM) observations were carried out at room temperature using sharp W tips. For the STM observations, the Ge NDs were fabricated on Si or $Si_{0.75}Ge_{0.25}$ on highly doped Si(001) substrates (electrical resistivity: 0.009-0.015 Ωcm) using ultrathin Si oxide film technique as follows. The Si substrates were cleaned by flashing at 1250˚C. In the case of the Ge NDs on Si, the cleaned surface was oxidized at 500˚C for 10 min under an oxygen pressure of 2×10^{-4} Pa to form the ultrathin Si oxide layer, and then Ge was deposited at 500˚C to form the Ge NDs. In the case of the Ge NDs on $Si_{0.75}Ge_{0.25}$, after obtaining cleaned Si surface, $Si_{0.75}Ge_{0.25}$ thin film was epitaxialy grown at 380˚C with a thickness of ~15 nm. Subsequently, the surface was oxidized at 450˚C and Ge was deposited at 500˚C.

Figures S1(a, b) and (c, d) show the STM images of the Ge NDs on Si and $Si_{0.75}Ge_{0.25}$, respectively. Regardless of the Ge composition of the underlying layer, the Ge NDs were randomly distributed with almost the same separation on the underlying layer. On the other hand, the cross-sectional view of the samples was observed by the cross-sectional annular dark field transmission electron microscopy (ADF-TEM) as shown in Figure 2(b) in the main text or the high-resolution TEM image.[1] As shown by the cross-sectional schematic of the Ge ND/SiGe or the Ge ND/Si films in Figure S1(e), the Ge ND layers were positioned almost periodically along the cross-plane direction although the Si oxide layers were relatively rough. As long as the system has the quasi-uniform ND separation, it is considered that the spatial distribution of NDs does not affect the simulation results in this paper based on the models (Figures S5(a) and S6(a)).

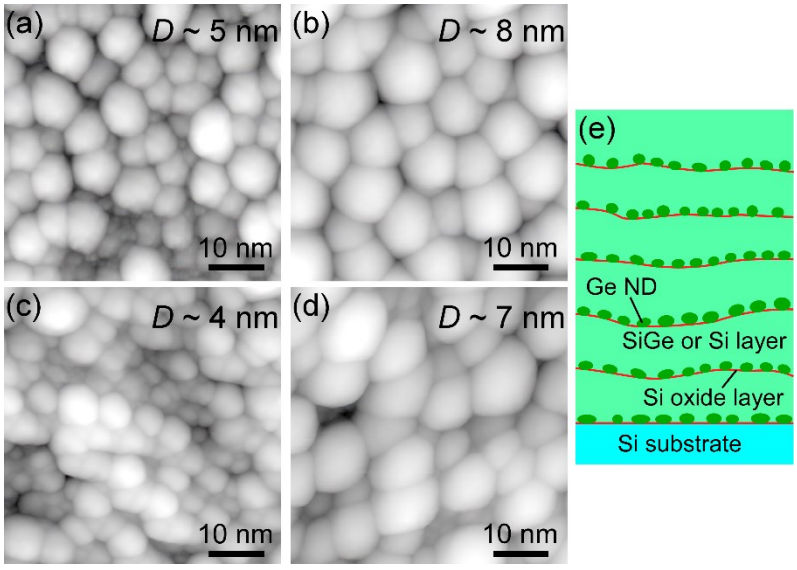

Figure. S1 (a-d) STM images of the Ge NDs on (a, b) Si and (c, d) $Si_{0.75}Ge_{0.25}$ layers. (e) Cross-sectional schematic of the Ge ND/SiGe or the Ge ND/Si films.

Section S2: The effect of the ultrathin Si oxide layer on the thermal resistance.

To investigate the effect of the Si oxide layer in $Si_{0.75}Ge_{0.25}$ films or Si films, we fabricated the epitaxial structures of $Si_{0.75}Ge_{0.25}$ or Si layer/the ultrathin Si oxide layer without NDs. In the Ge ND/Si films, the thermal resistance per one cycle structure (TRC) is constant with the change of the layer thickness L as shown in Figure 3b in the main text. Therefore, the thermal resistance of the Si oxide layer in Si layer was easily obtained from TRC of the stacked sample of Si layer/ultrathin Si oxide layer without NDs (namely, Ge ND (0 nm)/Si film), which is corresponding to the thermal resistance of ND layer (R_{ND}) at ND size of 0. On the other hand, as for the Si oxide layers in the $Si_{0.75}Ge_{0.25}$ layers, we obtained R_{ND} at ND size of 0 from the intercept of the L-dependence of thermal resistance of $Si_{0.75}Ge_{0.25}$ layer/ultrathin Si oxide layer without NDs as follows. We fabricated the epitaxial $Si_{0.75}Ge_{0.25}$ films on the Si oxide layers with various L, and measured their thermal resistances by 2ω method. The sample structure was composed of the $Si_{0.75}Ge_{0.25}$ layer and the Si oxide layer, which was not a repeatedly-stacked structure for simplicity unlike the Ge ND/$Si_{0.75}Ge_{0.25}$ films and the Ge ND/Si films, as shown in the inset of Figure S2. Figure S2 shows the dependence of the thermal resistance of these samples ($Si_{0.75}Ge_{0.25}$/ Si oxide films) on the L. The thermal resistance of the $Si_{0.75}Ge_{0.25}$/ Si oxide films monotonically increased with L increase. From the slope and the intercept of the thermal resistance, we obtained the thermal resistivity of the $Si_{0.75}Ge_{0.25}$ layer ($\rho_{layer} \sim 0.45 \pm 0.01$ mKW^{-1}) and the thermal resistance caused by the Si oxide layer ($R_0 \sim (7.7 \pm 0.6) \times 10^{-9}$ m^2KW^{-1}), respectively. The ρ_{layer} value agreed with the thermal resistivity of $Si_{0.75}Ge_{0.25}$ layer in the Ge ND/$Si_{0.75}Ge_{0.25}$ films (~0.38 ± 0.03 mKW^{-1}), and this R_0 value was corresponding to the R_{ND} at ND size of 0 in the case of Ge ND/$Si_{0.75}Ge_{0.25}$ films.

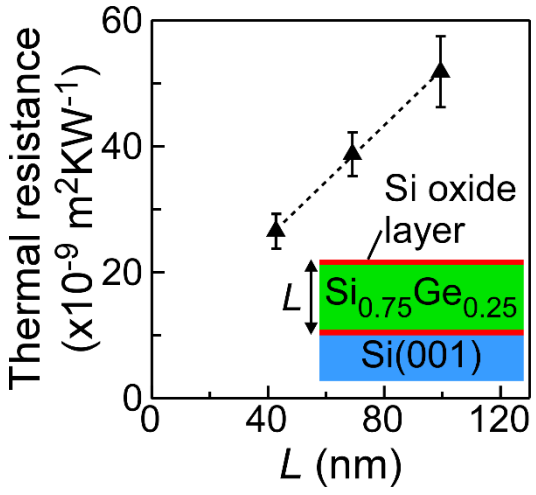

Figure S2. The L dependence of thermal resistance of the epitaxial $Si_{0.75}Ge_{0.25}$ / Si oxide films. The dotted line is the line-fit curve. The inset is a schematic of the sample structure.

Section S3: Assessment of interference effect.

In this paper, aiming at revealing the interference effect such as resonance feature, we compared the ballistic phonon transports with/without the interference effect. In this section, we explain the assessment of the interference effect by this comparison. In the virtual ballistic phonon transport without interference, we virtually considered the phonon particle traveling straight among interfaces. Therein, the reflection/scattering at the ND interface are only considered and there is no scattering in Si, as shown in Figure S3(b). In this transport without interference, the heat conduction is determined by the ND cross sectional ratio because NDs are target for the particles traveling straight. On the other hand, in the simulation of the coherent phonon transport, ballistic phonon transport with interference effect is reproduced (Figure S3(a)). Therefore, the difference between these two transports reveals the interference effect such as the resonance feature of the ND.

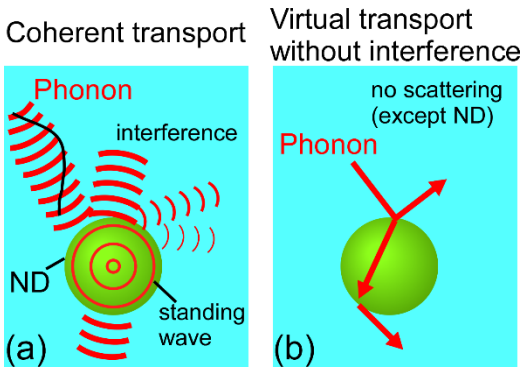

Figure S3. The schematics of (a) coherent phonon transport and (b) virtual phonon transport.

Section S4: Simulation of heat conduction in diffusive phonon transport.

To estimate the R_{ND} values, we used three dimensional heat conduction equation in the diffusive phonon transport. First, we formulated an update equation for an interface between two materials with different thermal conductivities (Figure S4) based on two fundamental equations on a thermal conduction equation and a thermal boundary resistance. For one-dimensional heat transfer problem, the thermal conduction equation is defined as

$$\frac{\partial T}{\partial t} = -\frac{\partial}{\partial x}\left(-k_x \frac{\partial T}{\partial x}\right) \quad \text{(S1)},$$

where T is absolute temperature, t is time, x is position, k_x is defined with thermal conductivity in x-direction, κ_x, specific heat, σ, and mass density, ρ, as $k_x = \kappa_x/(\sigma\rho)$. The thermal boundary resistance, r is also defined as

$$r = \frac{T - T'}{q} \quad \text{(S2)},$$

where T' and T are absolute temperatures just on the right and left sides of the interface, respectively (Figure S4), and q is heat flux. Since there are two unknowns, T'_i and T_i at the i-th node on the interface, we need to solve eq. (S1) simultaneously with the additional relation (eq. (S2)).

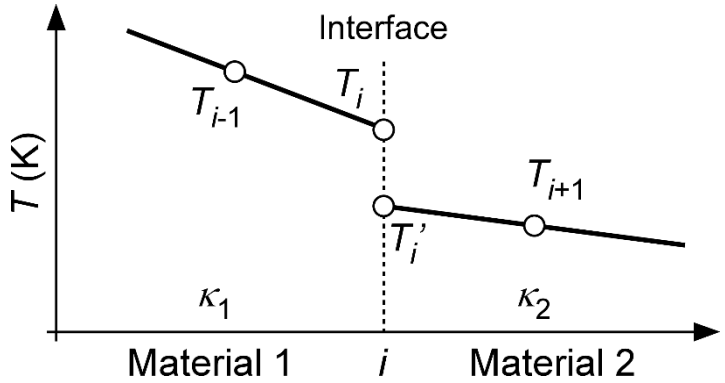

Figure S4. The schematic of the discontinuous temperature at an interface.

The heat conduction equation is discretized with the temperature at i-th node, T_i, as

$$\frac{T_i^{n+1} - T_i^n}{\Delta t} = \frac{1}{\Delta x}\left\{k_2 \frac{T_{i+1}^n - T'^n_i}{\Delta x} - k_1 \frac{T_i^n - T_{i-1}^n}{\Delta x}\right\} \quad \text{(S3)},$$

where the superscript n is the discretized time index, and k_1 and k_2 are the quantities $k_1 = \kappa_1/(\sigma_1\rho_1)$ and $k_2 = \kappa_2/(\sigma_2\rho_2)$ in material 1 and 2, respectively. On the interface at i-th node, the

temperature becomes discontinuous with the temperature difference, $T'_i - T_i$, which is expressed in terms of r as

$$T_i^n - T'^n_i = rq \tag{S4}.$$

Since $q = -\kappa_1 \partial T/\partial x$, eq. (S4) can be written as

$$T'^n_i = T_i^n - r\left(-\kappa_1 \frac{T_i^n - T_{i-1}^n}{\Delta x}\right) \tag{S5}.$$

Substituting eq. (S5) into eq. (S3), we obtain the explicit update equation as

$$T_i^{n+1} = T_i^n + \frac{\Delta t}{(\Delta x)^2}\left\{k_2\left(T_{i+1}^n - T_i^n\right) - k_1\left(T_i^n - T_{i-1}^n\right)\right\} - \frac{\Delta t k_2}{(\Delta x)^2}\frac{r\kappa_1}{\Delta x}\left(T_i^n - T_{i-1}^n\right) \tag{S6}.$$

The last term of eq. (S6) is the additional term by interfacial thermal resistance to thermal conduction equation.

For three dimensional problems, the heat flux is given by

$$\boldsymbol{q} = -\kappa_1 \nabla T \tag{S7}.$$

According to eq. (S4), we have

$$T^+ = T^- - r|\boldsymbol{q}| = T^- - r\kappa_1\left\{\left(\frac{\partial T}{\partial x}\right)^2 + \left(\frac{\partial T}{\partial y}\right)^2 + \left(\frac{\partial T}{\partial z}\right)^2\right\}^{\frac{1}{2}} \tag{S8}.$$

This equation yields discretized equation

$$T'^n_{i,j,k} = T_{i,j,k}^n - r\kappa_1\left\{\left(\frac{T_{i,j,k}^n - T_{i-1,j,k}^n}{\Delta x}\right)^2 + \left(\frac{T_{i,j,k}^n - T_{i,j-1,k}^n}{\Delta y}\right)^2 + \left(\frac{T_{i,j,k}^n - T_{i,j,k-1}^n}{\Delta z}\right)^2\right\}^{\frac{1}{2}} \tag{S9}.$$

Solving eq. (S9) simultaneously with three-dimensional Fourier's law, we can obtain the temperature distribution and R_{NDS}. In our simulation, since a major heat flux is in the z-direction (see Figure S5(a)), we made an approximation in (S9) as

$$T'^n_{i,j,k} \cong T_{i,j,k}^n - \frac{r\kappa_1}{\Delta z}\left(T_{i,j,k}^n - T_{i,j,k-1}^n\right) \tag{S10}$$

to save computational time.

Figure S5(a) shows the schematic of the simulation model. The ND size, D, and the ND coverage, θ, were measured by the scanning tunneling microscopy image. The relationship between D and θ is shown in Figure 5(d) in the main text. The ND separation A was also obtained from the relation $A^2 = \pi D^2/4\theta$. The cross-sectional length, l, is defined as $l = A$. The boundary conditions (BCs) of both ends of z axis were defined as the Dirichlet BCs for 400K (upper side) and 300K (lower side). The other BCs were the periodic BCs. The length of a piece of mesh for the simulation model is 0.2 nm. In these simulations, the thermal properties (the

thermal resistances and the interfacial thermal resistances) of the Si oxide layers in the Ge ND/Si films and the Ge ND/$Si_{0.75}Ge_{0.25}$ films are defined as the experimental R_{ND} values at D = 0 nm. The material parameters are summarized in Table S1.[2-4] Note that the interfacial thermal resistance of the $Si_{0.75}Ge_{0.25}$/Ge was estimated from that of the Si/Ge by assuming that the interfacial thermal resistance is linear to the atomic mass ratio,[4,5] and that the specific heat of $Si_{0.75}Ge_{0.25}$ was also estimated from that of Si and Ge by assuming the linear relationship between the specific heat and the Ge composition.

Table S1. The parameters of the materials used in the simulation.[2-4]

Material or interface	ρ (kgm^{-3})	σ ($JKg^{-1}K^{-1}$)	κ ($Wm^{-1}K^{-1}$)	Interfacial thermal resistance ($\times10^{-9}$ m^2KW^{-1})
Si	2330	703	156	–
Ge	5330	604	60	–
$Si_{0.75}Ge_{0.25}$	3080	310	7.7	–
Si/Ge	–	–	–	3.1
$Si_{0.75}Ge_{0.25}$/Ge	–	–	–	1.66

Figures S5(b) and (c) show the typical simulation results of the cross-sectional temperature distribution in the Ge ND/Si film and the Ge ND/$Si_{0.75}Ge_{0.25}$ film for D = 8.2 nm, respectively. From these results, we estimated the R_{ND} values by subtracting the thermal resistance of Si or $Si_{0.75}Ge_{0.25}$ layers from the total thermal resistance.

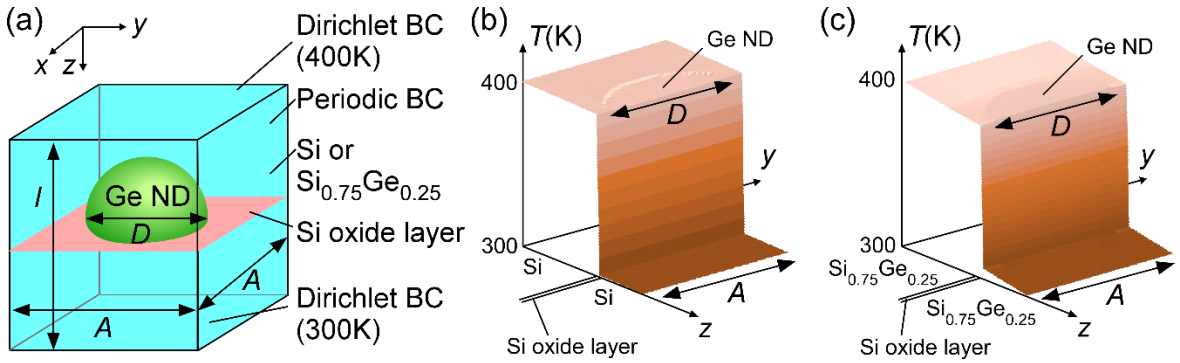

Figure S5. (a) The schematic of the simulation model. (b, c) The simulation results of the cross-sectional temperature distribution in (b) the Ge ND/Si film and (c) the Ge ND/$Si_{0.75}Ge_{0.25}$ film for D = 8.2 nm.

Section S5: Simulation in coherent phonon transport.

Elastic wave propagation in three dimensional media is simulated based on the linearized elasticity theory and a stress-stiffness tensor formulation. Finite-difference equations can be derived by simultaneously solving Hooke's law and the equation of motion in an elastic medium in the Cartesian system, i.e.,

$$\partial_t \boldsymbol{T} = [c]\nabla_s \dot{\boldsymbol{U}} \qquad \rho\partial_t \dot{\boldsymbol{U}} = \nabla \cdot \boldsymbol{T} + \boldsymbol{F} \tag{S11},$$

where $T = [T_{xx}, T_{yy}, T_{zz}, T_{yz}, T_{zx}, T_{xy}]^t$ is a stress vector given with the stress tensor components, $\dot{U} = [\dot{u}, \dot{v}, \dot{w}]^t$ is the velocity vector for the displacement vector $[u, v, w]$, $\boldsymbol{F}$ is the external force vector, $[c]$ is the stiffness tensor, ∂_t is temporal derivative, and $\nabla\cdot$ and ∇_S are the Auld operators[6] given by

$$\nabla\cdot = \nabla_s^t = \begin{bmatrix} \frac{\partial}{\partial x} & 0 & 0 & 0 & \frac{\partial}{\partial z} & \frac{\partial}{\partial y} \\ 0 & \frac{\partial}{\partial y} & 0 & \frac{\partial}{\partial z} & 0 & \frac{\partial}{\partial x} \\ 0 & 0 & \frac{\partial}{\partial z} & \frac{\partial}{\partial y} & \frac{\partial}{\partial x} & 0 \end{bmatrix} \tag{S12}.$$

Figure S6(a) shows the simulation model. The structural and material parameters are the same as those in Sec. S3, except for the cross-sectional length $l = 2A$ and the unknown ultrathin Si oxide layer. The stiffness tensor components were given as c_{11} = 166 GPa, c_{12} = 63.9 GPa for Si, and c_{11} = 129 GPa, c_{12} = 48.3 GPa for Ge. The component c_{44} was given by $c_{44} = (c_{11} - c_{12}) / 2$. For the Si oxide layer, the stiffness tensor components were assumed to be those for a bulk SiO_2: c_{11} = 87 GPa and c_{12} = 7 GPa. Twenty-layer perfectly matched layers (PMLs) were applied on top and bottom boundaries, and the periodic boundary conditions are applied to the lateral boundaries to mimic the ND layer. In this simulation, the computational region was discretized with the mesh sizes of 0.2 nm for $D \leq 8.2$ nm, 0.4 nm for D = 17.3 nm and 0.8 nm for D = 42.6 nm. Si oxide layer was treated as SiO_2 for simplicity because the stress tensor information of a few ML thick (not bulk material) Si oxide layer ($SiGeO_y$ or SiO_2-Ge)[7] are unknown. A Gaussian-enveloped coherent vibration pulse with the root-mean-square speed in Bose distributions at 300K with the Si Debye temperature of 645K were applied at each node on the input plane just below the upper PML above the Ge ND in Figure S6(a) independently to the static system, and the scattered wave transport was simulated. Figure S6(b) shows typical simulated wave distribution images at time of ~20, ~40, and ~60 fs after inputting coherent vibration pulse, indicating phonon wave with certain wavelengths passing through a ND.

We estimated transmitted energy at the output plane. The transmitted energy in the case of ND size at D, T_D, is written as

$$T_D = \int dt \int_{\text{ouput plane}} \dot{w} T_{zz} dS \qquad \text{(S13)},$$

where T_{zz} is zz-component of the stress tensor, w is z-component of the displacement vector, S is area of the cross section in the xy-plane. The reflected energy ratio was calculated using the equation of $1-T_D/T_0$, where T_0 is the transmitting wave energy without the Ge ND and the Si oxide layer.

Figure S6(c) shows the transmitted spectrum with various D. This result reveals that the transmitted wave spectrum is limited within the frequency range less than THz, implying that assuming the coherent phonon transport, the ND-size dependence of the experimental R_{ND} in the Ge ND/Si film case is due to low-frequency phonons. This is also consistent with phonon wave-packet dynamics,[8] which supports reliability of our simulation.

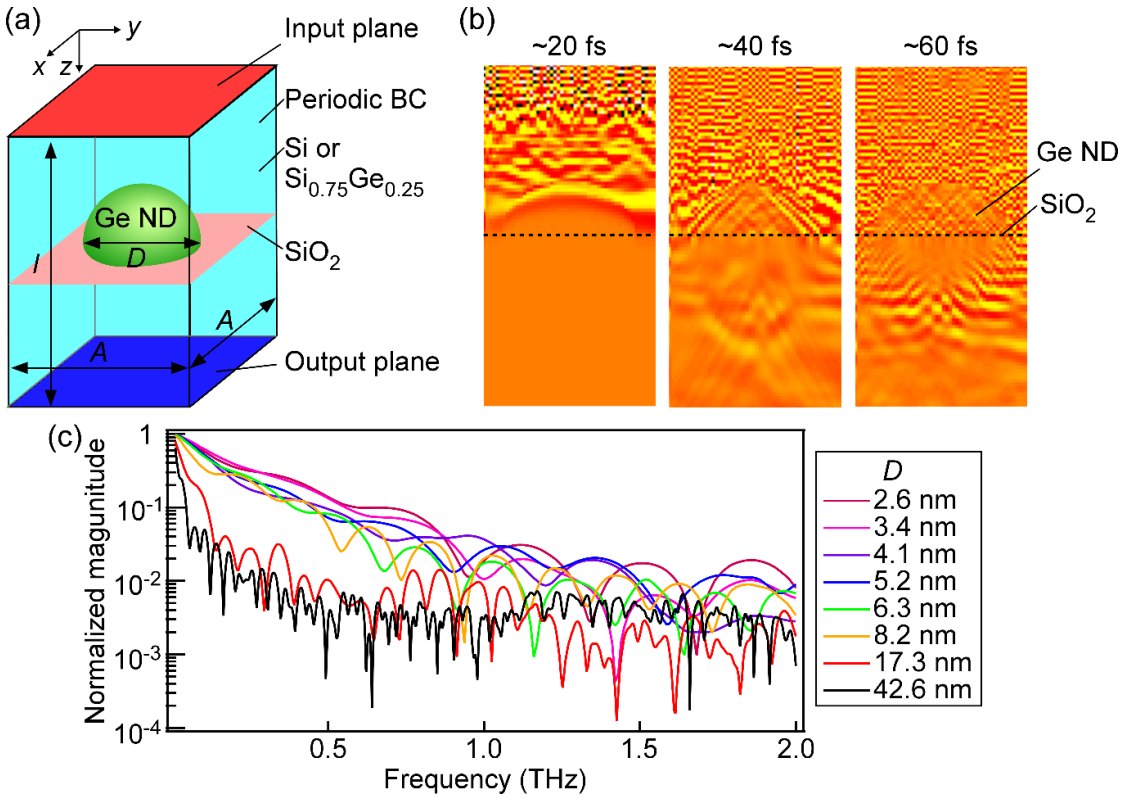

Figure S6. (a) The schematic of the simulation model. (b) Typical simulated wave distribution images (zz-component of the stress tensor) at time of ~20, ~40, and ~60 fs after inputting coherent vibration pulse in coherent phonon transport. (c) The transmitted spectrum.

REFERENCES

[1] S. Yamasaka, K. Watanabe, S. Sakane, S. Takeuchi, A. Sakai, K. Sawano, and Y. Nakamura, *Sci. Rep.*, 2016, **6**, 22838.

[2] C. J. Glassbrenner, and G. A. Slack, Phys. Rev., 1964, **134**, A1058.

[3] J. P. Dismukes, L. Ekstrom, E. F. Steigmeier, I. Kudman, and D. S. Beers, J. Appl. Phys., 1964, **35**, 2899.

[4] E. S. Landry, and A. J. H. McGaughey, Phys. Rev. B, 2009, **80**, 165304.

[5] J. A. Katerberg, C. L. Reynolds, Jr., and A. C. Anderson, Phys. Rev. B, 1977, **16**, 673.

[6] B. A. Auld, *Acoustic Fields and Waves in Solids 1*, John Wiley & Sons, 1973.

[7] N. Tanaka, S.-P. Cho, A. A. Shklyaev, J. Yamasaki, E. Okunishi, and M. Ichikawa, Appl. Surf. Sci., 2008, **254**, 7569.

[8] P. K. Schelling, S. R. Phillpot, and P. Keblinski, Appl. Phys. Lett., 2002, **80**, 2484.